

Inflow velocities of cold flows streaming into massive galaxies at high redshifts

Tobias Goerdt^{1*} and Daniel Ceverino²

¹*Institut für Astrophysik, Türkenschanzstraße 17, Universität Wien, 1180 Wien, Österreich*

²*Centro de Astrobiología (INTA-CSIC), Ctra de Torrejón a Ajalvir, km 4, 28850 Torrejón de Ardoz, Madrid, España*

Draft version 7 December 2024

ABSTRACT

We study the velocities of the accretion along streams from the cosmic web into massive galaxies at high redshift with the help of three different suites of AMR hydrodynamical cosmological simulations. The results are compared to free-fall velocities and to the sound speeds of the hot ambient medium. The sound speed of the hot ambient medium is calculated using two different methods to determine the medium’s temperature. We find that the simulated cold stream velocities are in violent disagreement with the corresponding free-fall profiles. The sound speed is a better albeit not always correct description of the cold flows’ velocity. Using these calculations as a first order approximation for the gas inflow velocities $v_{\text{inflow}} = 0.9 v_{\text{vir}}$ is given. We conclude from the hydrodynamical simulations as our main result that the velocity profiles for the cold streams are constant with radius. These constant inflow velocities have in units of the virial velocity a “parabola-like” dependency on the host halo mass that peaks at $M_{\text{vir}} = 10^{12} M_{\odot}$ and they follow a square root power law relation with respect to the redshift: $v_{\text{inflow}} \propto \sqrt{z+1} v_{\text{vir}}$.

Key words: cosmology: theory – galaxies: evolution – galaxies: formation – galaxies: high redshift – intergalactic medium – methods: numerical

1 INTRODUCTION

In the recent years it has been shown in theoretical work and in simulations (Fardal et al. 2001; Birnboim & Dekel 2003; Kereš et al. 2005, 2009; Dekel & Birnboim 2006; Ocvirk, Pichon & Teyssier 2008; Dekel et al. 2009a, 2013) that massive galaxies in the high redshift regime ($z \gtrsim 1.5$), acquire their baryons primarily via cold narrow streams of relatively dense and pristine gas with temperatures around 10^4 K. These cold flows penetrate through the diffuse shock-heated medium. Their activity peaks around redshift 3. Having reached the inner parts of the host halo their gas will eventually form a dense, unstable, turbulent disc with a bulge where rapid star formation is triggered (Agertz, Teyssier & Moore 2009, 2011; Dekel, Sari & Ceverino 2009b; Ceverino, Dekel & Bournaud 2010; Krumholz & Burkert 2010; Ceverino et al. 2012, 2014, 2015; Cacciato, Dekel & Genel 2012; Genel, Dekel & Cacciato 2012; Genzel et al. 2011; Mandelker et al. 2014). The timescales for star formation as well as the star formation

rate both depend crucially on the gas accretion rate, which in turn depends on the speed of the infalling gas when it reaches the halo centre. So doubling the infall velocity would also result in doubling the star formation rate for the same amount of infalling mass, which highlights the importance of the inflow velocity.

Processes of observing the cold accretion stream paradigm in the real universe are ongoing. Goerdt et al. (2012) made theoretical predictions about the likelihood of observing these streams in absorption. Striking features in absorption have indeed been observed (Bouché et al. 2013). Ibata et al. (2013) found the existence of a planar subgroup of satellites in the Andromeda galaxy (M 31), comprising about half of the population. Goerdt, Burkert & Ceverino (2013) demonstrated that this vast thin disk of satellites can naturally be explained within the cold stream framework and should therefore be interpreted as indirect observational evidence for the cold stream paradigm.

Goerdt et al. (2010) used the cold stream model to explain the observational phenomenon of Ly α -blobs (LABs). They deployed cosmological hydrodynamical AMR simulations to predict the characteristics of Ly α emission from the cold gas streams. These authors pointed out that in their

* tobias.goerdt@univie.ac.at

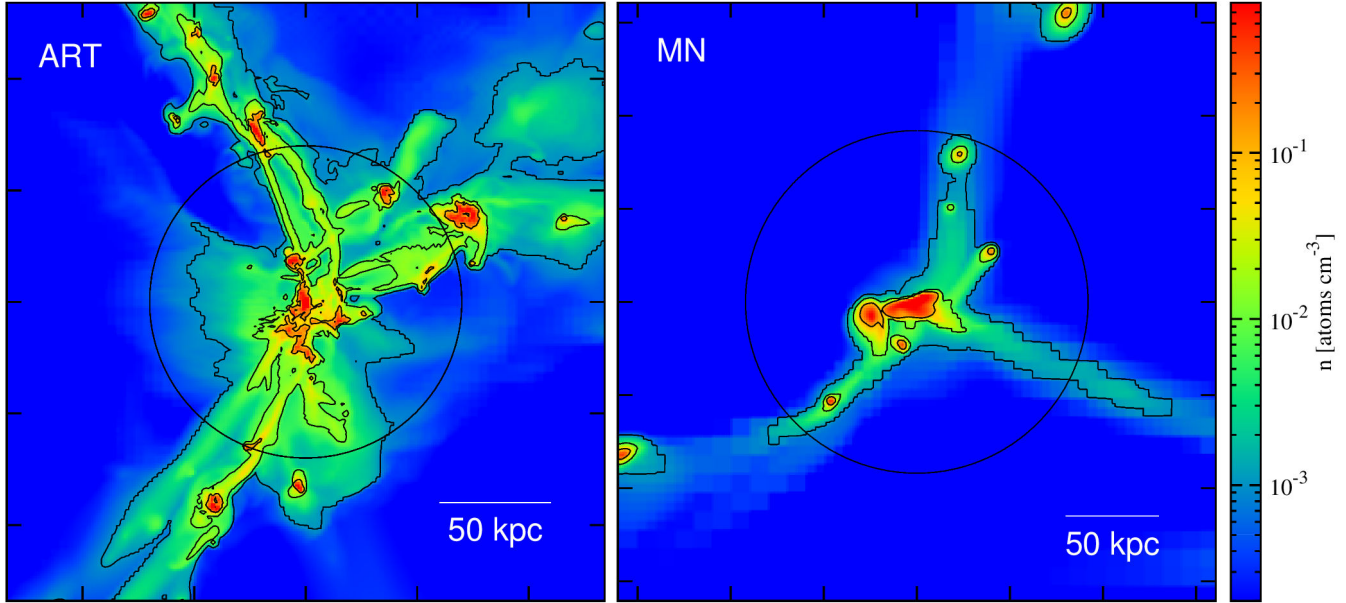


Figure 1. Two simulated galaxies from ART and MN. The colour refers to the maximum gas density along the line of sight. Contour lines are at $n = 0.1, 0.01$ and 0.001 cm^{-3} , respectively. The circles show the virial radii. Left: a typical ART galaxy (resolution 70 pc) at $z = 2.3$, with $M_{\text{vir}} = 3.5 \times 10^{11} M_{\odot}$. Right: one of the MN galaxies (resolution 1 kpc) at $z = 2.5$, with $M_{\text{vir}} = 10^{12} M_{\odot}$. In both cases, the inflow is dominated by three cold narrow streams that are partly clumpy. The density in the streams is $n = 0.003 - 0.1 \text{ cm}^{-3}$, with the clump cores reaching $n \sim 1 \text{ cm}^{-3}$.

simulations the velocities of the cold streams are constant. So the potential energy of the inflowing gas is not converted into kinetic energy. Subsequently they concluded that it is the release of gravitational energy as the gas is flowing down the potential gradient toward the halo centre which powers the $\text{Ly}\alpha$ luminosity. The potential energy of the inflowing gas is released as $\text{Ly}\alpha$ radiation. Faucher-Giguere et al. (2010) tested the results of Goerdt et al. (2010). They analysed cosmological smoothed particle hydrodynamics simulations to predict the $\text{Ly}\alpha$ cooling emission of forming galaxies with the help of a $\text{Ly}\alpha$ radiative transfer code. In contrast to Goerdt et al. (2010) they mention that a scenario in which the cold streams free-fall into the haloes and release little energy before hitting the central disk in a strong shock, may be supported by their results. Later also Rosdahl & Blaizot (2012) addressed the same question independently. For this purpose they ran and analysed cosmological radiation-hydrodynamics simulations. They looked at phase diagrams for their haloes of gas speed versus radius in which they were able to distinguish several cold streams. They produced corresponding free-fall profiles (i.e. the speeds that the streams would follow were they in free-fall). In contrast to Goerdt et al. (2010) they concluded that the streams are close to free-fall.

Wetzel & Nagai (2014) explored systematically the physics that governs cosmic accretion into haloes and their galaxies. They analysed a suite of cosmological simulations that incorporate both dark matter and gas dynamics with differing treatments of gas cooling, star formation and thermal feedback to explore the physics that governs the accretion of dark matter and baryons into halos and their galaxies. They presented average radial velocities of the inflowing material (their figures 4 and 6, bottom panels). The inflow

velocities presented there decrease with decreasing radius (roughly a decrease of 65% between $1 r_{\text{vir}}$ and the centre of the host).

In this paper we look at the velocity profiles of the gas inflow, both as a function of radius, mass and redshift for the three constituents of the simulations, namely gas, stars and dark matter. The paper is organised as follows: in section 2 we present the three suites of simulations used for the following analysis, in section 3 we present our toy models. In section 4 we discuss the velocity profiles of the inflow along the streams and in section 5 we draw our conclusions.

2 SIMULATIONS

We use snapshots of galaxies from three different sets of simulations, all three employing Eulerian AMR (Adaptive Mesh Refinement) hydrodynamics in a cosmological setting. The ART (Ceverino, Dekel & Bournaud 2010; Ceverino et al. 2012; Dekel et al. 2013; Ceverino et al. 2015) suite consists of several zoom-in simulations with a maximum resolution of $35 - 70 \text{ pc}$ at $z = 2$. The simulation zooms in on individual galaxies that reside in dark-matter haloes which have masses of $(0.13 - 1.60) \times 10^{12} M_{\odot}$ at $z = 2.3$. This ART suite has got an extension that we will also use, the ARP suite of simulations which includes radiation pressure feedback (Ceverino et al. 2014). This second suites consist of individual galaxies that reside in dark-matter haloes of masses $(1 - 8) \times 10^{11} M_{\odot}$ at $z = 2.0$. The third simulation is the Horizon-MareNostrum (hereafter MN) simulation (Ocvirk, Pichon & Teyssier 2008) containing dozens of massive galaxies in a cosmological box of side 71 Mpc with a maximum resolution of $\leq 1 \text{ kpc}$.

Density maps of galaxies of the MN as well as the ART suite are shown in figure 1. They demonstrate the dominance of typically three, narrow cold streams, which come from well outside the virial radius along the dark-matter filaments of the cosmic web, and penetrate into the discs at the halo centres. The streams are partly clumpy and partly smooth, even in the simulation of higher resolution. The typical densities in the streams are in the range $n = 0.01 - 0.1 \text{ cm}^{-3}$, and they reach $n = 0.1 - 1 \text{ cm}^{-3}$ at the clump centres and in the central disk.

2.1 High-resolution ART simulations

These simulations were run with the AMR code ART (Adaptive Refinement Tree; Kravtsov, Klypin & Khokhlov 1997; Kravtsov 2003) with a spatial resolution better than 70 pc in physical units. It incorporates gas cooling, photoionisation heating, star formation, metal enrichment and stellar feedback (Ceverino & Klypin 2009) which are relevant physical processes for galaxy formation. For the gas density, temperature, metallicity, and UV background in any given cell cooling rates were computed using CLOUDY (Ferland et al. 1998). It is assumed that cooling takes place at the centre of a cloud of thickness 1 kpc (Ceverino-Rodriguez 2008; Robertson & Kravtsov 2008). Metallicity dependent, metal-line cooling is also included, assuming a relative abundance of elements equal to the solar composition. The code implements a “constant” feedback model, in which the combined energy from stellar winds and supernova explosions is released as a constant heating rate over 40 Myr (the typical age of the lightest star that can still explode in a type-II supernova). Photo-heating is taken into account self-consistently with radiative cooling. A uniform UV background (Haardt & Madau 1996) is assumed, ignoring local sources. The self-shielding of dense, galactic neutral hydrogen from the cosmological UV background is mimicked by assuming a substantially suppressed UV background ($5.9 \times 10^{26} \text{ erg s}^{-1} \text{ cm}^{-2} \text{ Hz}^{-1}$, the value of the pre-reionisation UV background at $z = 8$) for the gas at densities above $n = 0.1 \text{ cm}^{-3}$.

Our special version of the ART code has a unique feature for the purpose of simulating the detailed structure of the streams. It allows gas cooling to well below 10^4 K so enabling the formation of high densities in pressure equilibrium with the hotter and more dilute medium. A non-thermal pressure floor has been implemented to ensure that the Jeans length is resolved by at least seven resolution elements and thus prevent artificial fragmentation on the smallest grid scale (Truelove et al. 1997; Robertson & Kravtsov 2008; Ceverino, Dekel & Bournaud 2010). It is effective in the dense ($n > 10 \text{ cm}^{-3}$) and cold ($T < 10^4 \text{ K}$) regions inside galactic disks.

The equation of state remains unchanged at all densities. Stars form according to a stochastic model that is consistent with the Kennicutt (1998) law. This happens in cells where the gas temperature is below 10^4 K and the gas density is above a threshold of $n = 1 \text{ cm}^{-3}$. We use the IMF from Miller & Scalo (1979) that is also matching the results of Woosley & Weaver (1995). Metals from supernovae type II and type Ia enrich the ISM. They are released from each star particle by SNII at a constant rate for 40 Myr after its birth. The metal ejection by SNIa assumes an exponentially

declining SNIa rate from a maximum at 1 Gyr. The code treats the advection of metals self-consistently and it distinguishes between SNII and SNIa ejecta (Ceverino-Rodriguez 2008).

2.1.1 Simulations including radiation pressure (ARP)

The ARP suite of simulations (Ceverino et al. 2014) is a further development of last subsection’s ART suite: Apart from the features already presented there, it also includes the effects of radiation pressure by massive stars. The radiation pressure was modelled as a non-thermal pressure that acts only in dense and optically thick star-forming regions in a way that the ionising radiation injects momentum around massive stars, pressurising star-forming regions (Agertz et al. 2013, their appendix B). The adaptive comoving mesh has been refined in the dense regions to cells of minimum size between 17-35 pc in physical units. The DM particle mass is $8.3 \times 10^4 M_\odot$. The particles representing star clusters have a minimum mass of $10^3 M_\odot$, similar to the stellar mass of an Orion-like star cluster.

2.2 Ramses Horizon-MareNostrum simulation

The AMR code RAMSES (Teyssier 2002) is used for this simulation. Its spatial resolution in physical units is $\sim 1 \text{ kpc}$. We included UV heating via a background model (Haardt & Madau 1996). Supernovae feedback and metal enrichment is modelled in a simple way using the implementation described in Dubois & Teyssier (2008). Cooling rates are calculated assuming ionisation equilibrium for H and He, for collisional- and photo-ionisation (Katz, Hernquist & Weinberg 1992). Metal cooling is assumed to be proportional to the metallicity, relative to the solar abundance (Grevesse & Sauval 1998). It is calculated with the help of tabulated CLOUDY rates. Unlike in the ART or ARP simulations, no cooling below $T < 10^4 \text{ K}$ is computed, and no self-shielding of the UV flux is assumed.

For high-density regions, we consider a polytropic equation of state with $\gamma_0 = 5/3$ to model the complex, turbulent multi-phase structure of the inter-stellar medium (ISM) (Yepes et al. 1997; Springel & Hernquist 1999) in a simplified form (see Schaye & Dalla Vecchia 1999; Dubois & Teyssier 2008). The ISM is defined as gas with hydrogen density greater than $n_H = 0.1 \text{ cm}^{-3}$. This definition is one order of magnitude lower than the one of the ART and ARP simulations. Star formation has only for ISM gas been included. It is modelled by spawning star particles at a rate consistent with the Kennicutt (1998) law derived from local observations of star forming galaxies.

The RAMSES code implements a pressure floor in order to prevent artificial fragmentation, by keeping the Jeans lengthscale, $\lambda_J \propto T n^{-2/3}$, larger than 4 grid-cell sides everywhere. In any case where $n > 0.1 \text{ cm}^{-3}$, a density dependent temperature floor was imposed. It mimics the average thermal and turbulent pressure of the multiphase ISM (Springel & Hernquist 1999; Dalla Vecchia & Schaye 2008). In our case, we allow the gas to heat up above this temperature floor and cool back. The temperature floor follows a polytropic equation of state with $T_{\text{floor}} = T_0 (n/n_0)^{\gamma_0 - 1}$, where $T_0 = 10^4 \text{ K}$ and $n_0 = 0.1 \text{ atoms cm}^{-3}$. The resulting

label	suite	$M_{\text{vir}} [10^{12} M_{\odot}]$	z	N_{gal}
10^{13}	MN	10.47 ± 0.56	1.57	12
10^{13}	MN	10.49 ± 0.93	2.46	12
5×10^{12}	MN	5.00 ± 0.045	1.57	12
5×10^{12}	MN	5.48 ± 0.26	2.46	11
10^{12}	MN	1.03 ± 0.003	1.57	8
10^{12}	MN	1.01 ± 0.004	2.46	12
10^{12}	MN	1.03 ± 0.006	4.01	9
10^{11}	MN	0.099 ± 0.000	1.57	12
10^{11}	MN	0.099 ± 0.000	2.46	7
10^{11}	MN	0.099 ± 0.000	4.01	12
1.9×10^{12}	ART	1.907 ± 0.217	1.14 ± 0.02	34
1.3×10^{12}	ART	1.286 ± 0.093	1.60 ± 0.02	73
8.6×10^{11}	ART	0.863 ± 0.046	2.25 ± 0.02	109
3.9×10^{11}	ART	0.391 ± 0.034	3.40 ± 0.04	119
7.1×10^{11}	ARP	0.707 ± 0.055	1.14 ± 0.02	41
6.7×10^{11}	ARP	0.672 ± 0.049	1.58 ± 0.02	47
4.9×10^{11}	ARP	0.491 ± 0.028	2.21 ± 0.03	57
2.9×10^{11}	ARP	0.290 ± 0.019	3.27 ± 0.05	62
2.6×10^{11}	ARP	0.260 ± 0.010	1.13 ± 0.02	40
2.4×10^{11}	ARP	0.242 ± 0.010	1.59 ± 0.02	50
1.6×10^{11}	ARP	0.160 ± 0.007	2.29 ± 0.03	60
7.3×10^{10}	ARP	0.073 ± 0.004	3.53 ± 0.05	66

Table 1. The different bins of galaxies which are used throughout this paper. ‘Label’ denotes the tag a bin is labelled with in any of the figures. It usually is a mass very close to the ensemble’s actual mean virial mass. ‘Suite’ indicates the simulation set the bin consists of. M_{vir} gives the actual mean virial mass of the ensemble together with its standard deviation. z is the mean redshift of the ensemble together with its standard deviation. We do not combine galaxies from different MN snapshots therefore the standard deviation of the redshift of any of the MN bins is always zero. N_{gal} is the number of galaxies in the respective bin.

pressure floor is given by $P_{\text{floor}} = n_{\text{H}} k_{\text{B}} T_{\text{floor}}$. For each stellar population, 10% of the mass is assumed to go through a supernovae type II event after 10 Myr. For each supernova, 10% of the ejected mass is assumed to be pure metals. The energy and the metals produced by the supernova event are released in a single impulse. The remaining 90% of the ejected mass keep the metallicity of their star at birth. Feedback through supernovae type Ia has not been considered.

The initial conditions were constructed assuming a Λ CDM universe with $\Omega_{\text{M}} = 0.3$, $\Omega_{\Lambda} = 0.7$, $\Omega_{\text{b}} = 0.045$, $h = 0.7$ and $\sigma_8 = 0.9$ in a periodic box of 71 Mpc. The adaptive-resolution rules in this simulation were the same everywhere, with no zoom-in resimulation of individual galaxies. The dark matter particle mass is $1.16 \times 10^7 M_{\odot}$, the star particle mass is $2.05 \times 10^6 M_{\odot}$, the smallest cell size is 1.09 kpc physical, and the force softening length is 1.65 kpc.

We will show averaged results for an ensemble of galaxies having very similar masses and redshifts. In table 1 we show a summary of the various bins of galaxies we use. Since we have better statistics for the MN simulation we could bin galaxies from a narrower mass range therefore the standard deviations of the mean mass of a MN bin is usually much smaller. To partly compensate for that we combine ART as well as ARP galaxies from adjacent redshifts increasing the statistics but introducing a standard deviation into the mean redshift of the bin.

3 ANALYTICAL MODELS

Naively one would expect the gas inflow velocities to obey one of the following two quantities: either free-fall or the sound speed of the hot ambient medium. The underlying assumption of the first case is that the gas flows freely within the gravitational potential into its host and is otherwise completely unconstrained. In the second case one assumes that the velocity of the gas will be fundamentally limited by the sound speed of the hot ambient medium through the effect of shocks which occur within the streams themselves as well as at the boundary layers between the streams and the hot ambient medium as soon as the velocity of the inflowing gas reaches the sound speed of this ambient medium.

3.1 Free-fall

Free-fall profiles cannot be calculated analytically. To evaluate them numerically we follow the method laid out by Rosdahl & Blaizot (2012) which we will quickly outline here: A static, spherically symmetric potential is assumed. We integrate the free-fall speeds $v_{\text{ff}}(r)$ from a starting position r_0 and a starting velocity $v_{\text{init}} = v_{\text{ff}}(r_0)$ towards the halo centre using

$$dv_{\text{ff}}(r) = \frac{1}{v_{\text{ff}}(r)} \frac{G M(< r)}{r^2} dr, \quad (1)$$

where r is radius, $M(< r)$ is the total halo mass within r and G is the gravitational constant. In practice we divide the host halo into spherical bins at radial positions r_i , where an increasing i corresponds to a decreasing radius, and solve the above equation by recursively computing

$$v_{\text{ff}}(r_{i+1}) = v_{\text{ff}}(r_i) + \frac{1}{v(r_i)} \frac{G M(< r_{i+1})}{r_{i+1}^2} (r_{i+1} - r_i). \quad (2)$$

The underlying mass distribution $M(< r_{i+1})$ is measured from the outputs of the hydrodynamical simulations as described in section 2. We choose an initial position ($r_0 = 1.7 r_{\text{vir}}$) as well as an initial inward velocity ($v_{\text{init}} = 0$) and integrate the path of the free-falling gas iteratively until a very small radius ($0.1 r_{\text{vir}}$) is reached. The free-fall profiles usually show a strongly increasing velocity with decreasing radius. The results of the calculations are presented in detail in section 4. We will see that these predictions violently disagree with the results from the hydrodynamical simulations.

3.2 Sound speed of the ambient medium

The sound speed c_s of the hot ambient halo gas on the other hand can be calculated analytically. Sound speed as such equals to

$$c_s(\vec{r}) = \sqrt{\frac{\gamma k_{\text{B}} T(\vec{r})}{m_{\text{p}} \mu_{\text{av}}}}, \quad (3)$$

with γ being the ratio of the heat capacity at constant pressure to the heat capacity at constant volume, which is usually a constant ($\sim 5/3$). k_{B} is Boltzmann’s constant, m_{p} is the proton mass, μ_{av} is the mean molecular weight (for ionised gas $\mu_{\text{av}} = 0.61$) and $T(\vec{r})$ is temperature of the gas as a function of position.

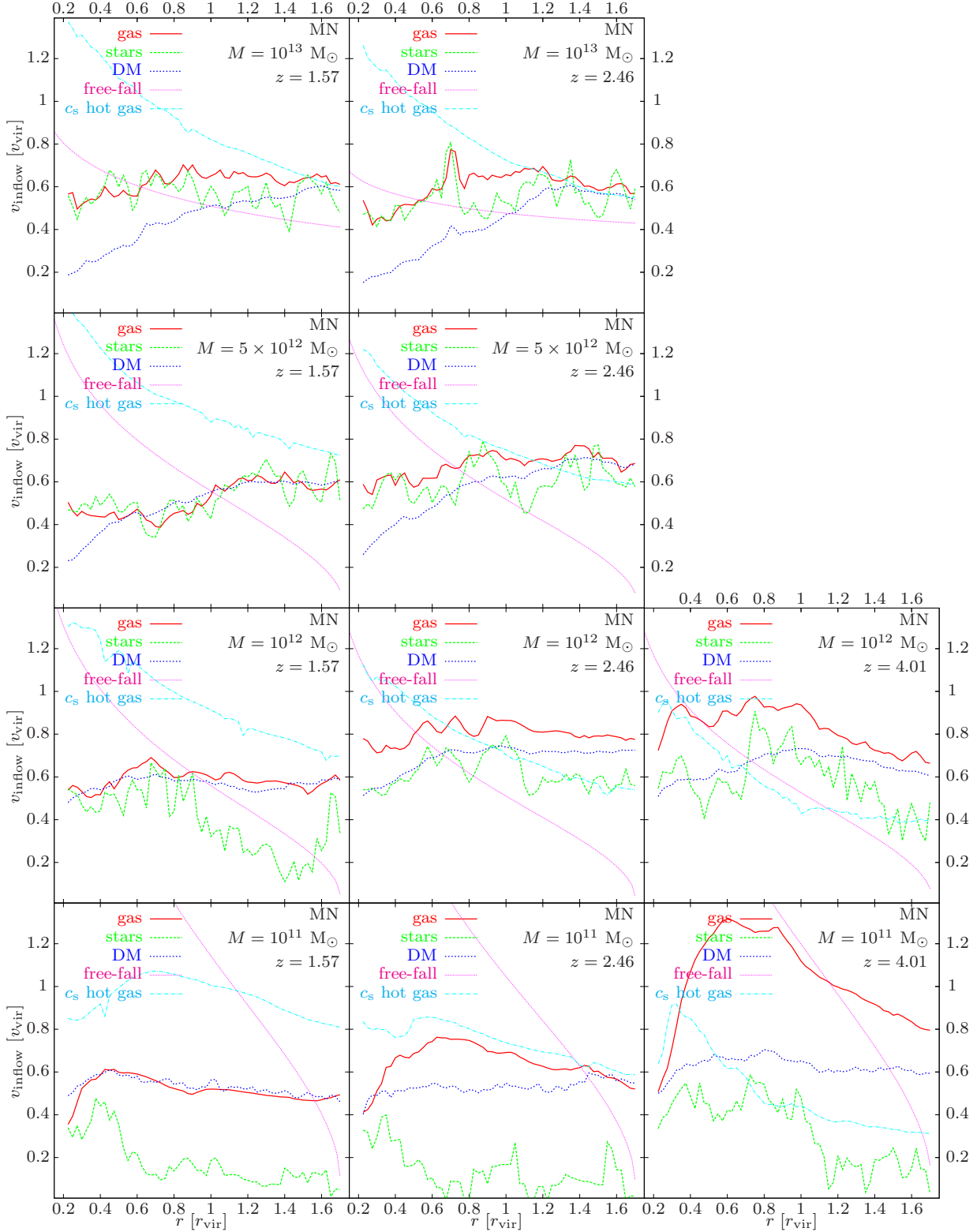


Figure 2. Mass weighted averages of the inflow velocities as a function of radius for the MN simulations. The different panels indicate a variety of different halo masses and redshifts. Corresponding free-fall profiles are over-plotted in dotted magenta and profiles of the sound speed of the hot ambient halo gas in dash-dotted turquoise. For low mass haloes ($M_{\text{vir}} \leq 10^{12} M_{\odot}$) at all redshifts the velocities are roughly constant with radius. For high mass haloes ($M_{\text{vir}} \geq 5 \times 10^{12} M_{\odot}$) the inflow velocities increase slightly with increasing radius. Subsequently no sign of free-fall can be seen in any of the bins. In the very high redshift and low mass cases one sees an increase of velocity with decreasing radius down to $0.6 r_{\text{vir}}$ from where the velocity is decreasing again. These shapes are typical for high redshift low mass haloes. In units of the virial velocity the average inflow velocity stays roughly constant with varying host halo mass, it increases with an increase in redshift.

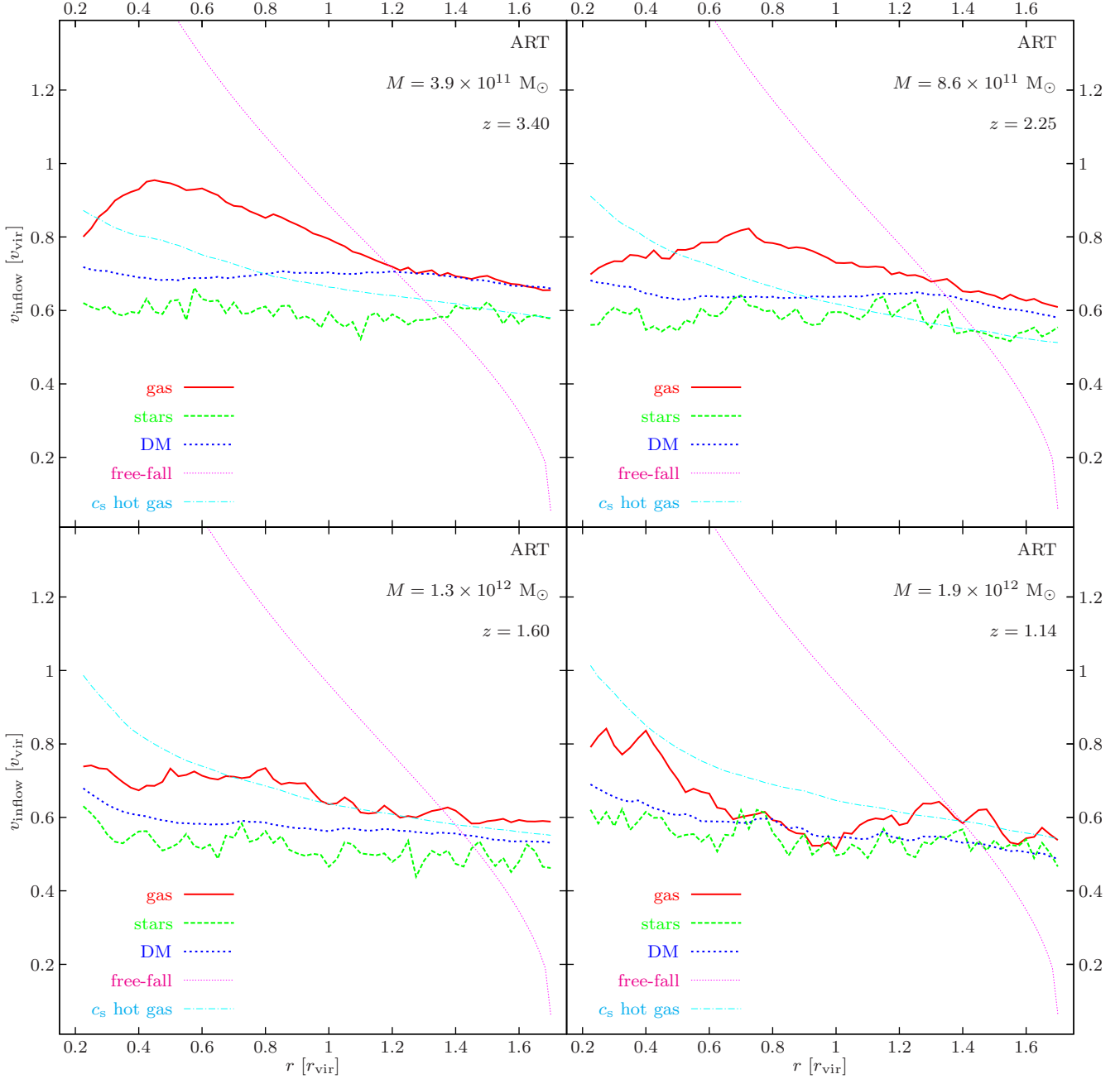


Figure 3. Mass weighted averages of the inflow velocities as a function of radius for the ART simulations. Free-fall profiles are over-plotted in dotted magenta and the sound speeds of the hot ambient halo gas in dash-dotted turquoise. The inflow velocities of the gas increase slightly with decreasing radius. The total increase over the whole radius range is usually roughly 50%. These increases however are not consistent with free-fall as the corresponding profiles show. The sound speeds of the hot halo gas are a much better proxy, at least at high redshift. In the higher redshift cases one sees an increase of velocity with decreasing radius down to $\sim 0.5 r_{\text{vir}}$ from where the velocity is decreasing again. A shape like that is typical for low mass haloes at high redshift, it originates in the loss of angular momentum during the “strong-torque phase” (Danovich et al. 2014).

3.2.1 Approximated constant halo gas temperature

For a first order approximation the temperature of the ambient halo gas is assumed to be equal to the virial temperature of the host halo. It is constant with position and given by

$$T_{\text{vir}} = \frac{G M_{\text{vir}} m_{\text{p}} \mu_{\text{av}}}{2 r_{\text{vir}} k_{\text{B}}}. \quad (4)$$

G is the gravitational constant, M_{vir} is the virial mass of the host halo and r_{vir} its virial radius. These three quantities are related via

$$v_{\text{vir}} = \sqrt{\frac{G M_{\text{vir}}}{r_{\text{vir}}}}. \quad (5)$$

After inserting the expressions for T_{vir} and v_{vir} into equation (3) we get an expression for the sound speed. Assuming that

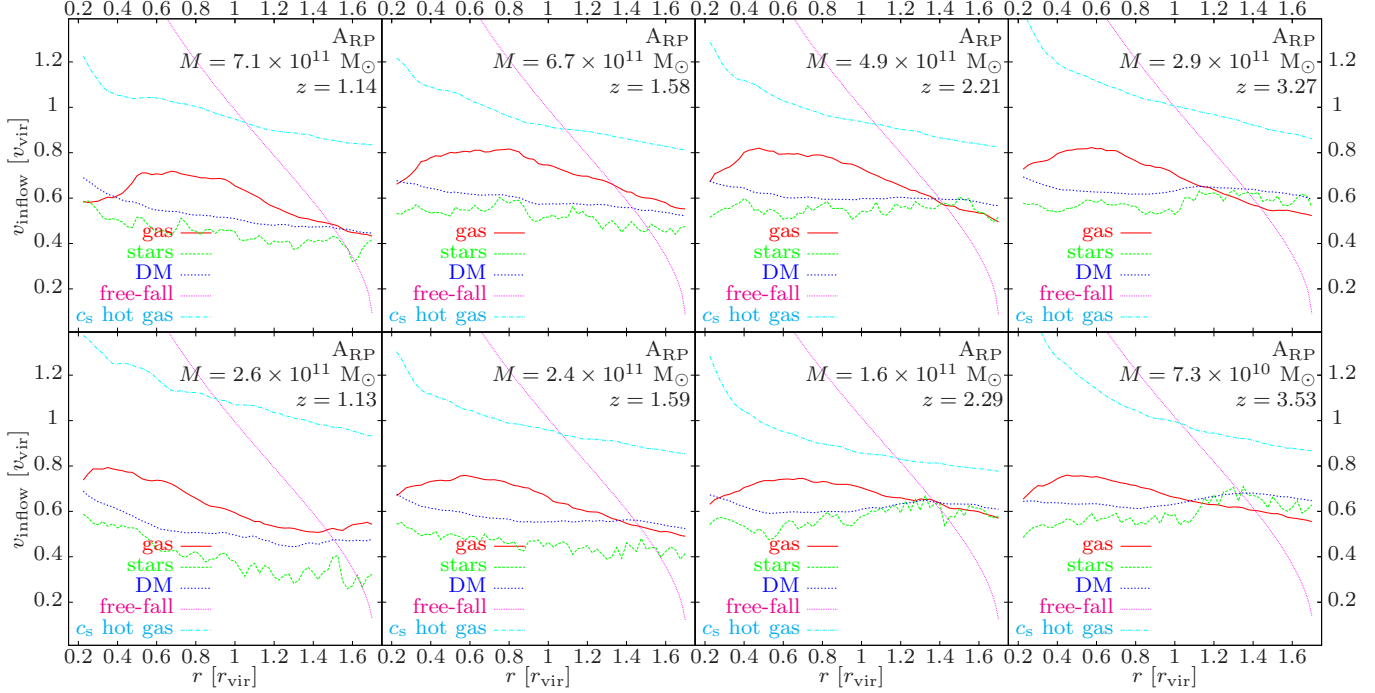


Figure 4. Mass weighted averages of the inflow velocities as a function of radius for the ARp simulations. Free-fall profiles are over-plotted in dotted magenta and the sound speeds of the hot ambient halo gas in dash-dotted turquoise. Again the inflow velocities of the gas increase with decreasing radius in most cases. These increases are again not consistent with free-fall. In most cases one sees an increase of velocity with decreasing radius down to $\sim 0.5 r_{\text{vir}}$ from where the velocity is decreasing again. A shape like that is typical for low mass haloes at high redshift.

the velocity of the gas in the cold streams indeed equals to the sound speed of the ambient medium, because the shocks which occur as soon as the inflow velocity reaches the sound speed will fundamentally limit the velocity of the gas one gets a first order approximation for the inflow velocity:

$$v_{\text{inflow}} = 0.913 v_{\text{vir}} \quad (6)$$

In this approximation the inflow velocity is constant with radial distance from the host halo. We will come back to this statement at the end of section 4 where we will see that this particular equation tends to be accurate for very high redshift haloes ($z \gtrsim 4.0$) and more importantly that the inflow velocity is in general indeed constant with radius.

3.2.2 Simulated halo gas temperature

A more sophisticated measure of the ambient medium's temperature is not to approximate the gas temperature anymore, but to measure it directly from the hydrodynamic simulations as a function of position. Since we assume spherical symmetry it is sufficient to measure it as a function of radial distance from the host halo centre. When looking at the simulations one has to carefully discriminate between the gas of the ambient medium which is hot and the gas flowing into the host as part of the cold streams which is cold. Only the temperatures of the ambient medium will determine the velocity of the cold streams. To distinguish between cold streams on the one hand and hot halo gas on the other hand we adopt the following temperature cut: Temperatures are defined as 'hot' in this sense if they are at least $> 0.2 T_{\text{vir}}$ or $> 3 \times 10^4$ K whatever is the higher value. The mass weighted

average temperatures of the hot ambient halo gas only are then taken in spherically symmetric bins at different radii r to get a numerical temperature profile $T(r)$. Inserting this numerical profile for the temperature into equation (3) we get a sound speed profile for each set of simulated galaxies that are listed in table 1. The sound speed profiles are presented together with the results from the hydrodynamical simulations in section 4. For the MN simulations at intermediate to high masses ($M_{\text{vir}} \geq 10^{12} M_{\odot}$), the sound speed is increasing with decreasing redshift almost as sharply as the free-fall profiles. In these regions of the parameter space it can only serve as a slightly better proxy for the inflow velocity than free-fall. In all four bins of the ART simulations the sound speed profiles increase slightly with decreasing radius. Here the sound speeds match the simulations very precisely. The profiles increase slightly with decreasing radius also in the ARp simulations. Their shape is very similar to the actual simulation values but the sound speeds are usually 50% higher than the simulation values. To summarise: the sound speed of the hot ambient halo gas is a better proxy for the velocity of the inflow than free-fall. It is more precise at low masses ($M_{\text{vir}} \leq 10^{12} M_{\odot}$) and gives very good results for the ART suite of simulations. However it is only an incomplete prescription for the inflow velocity.

4 INFLOW VELOCITIES

The analysis of the hydrodynamical simulation starts by compiling averaged inflow velocity profiles for all simulated galaxies listed in table 1. Since we want to look at the ve-

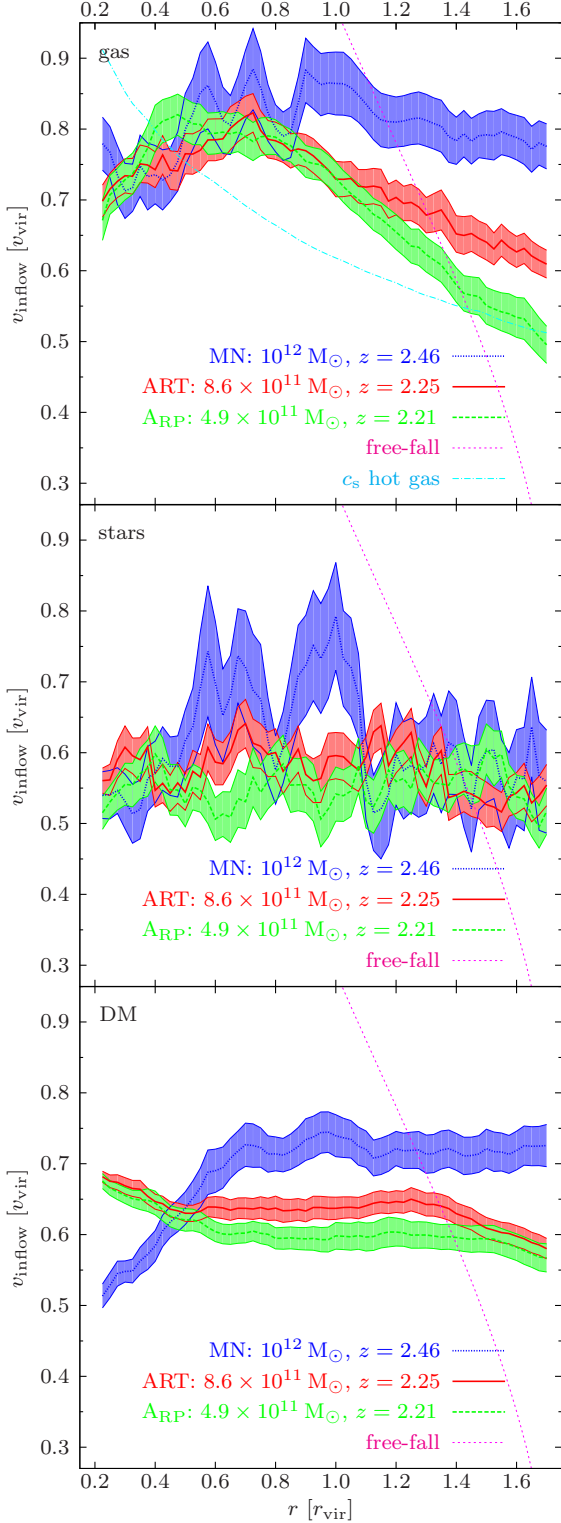


Figure 5. Direct comparison between the MN (dotted blue), the ART (solid red) and the A_{RP} (long-dashed green) suite of simulations. The inflow velocities as a function of radius are shown together with their 1σ standard deviation lines. Over-plotted are a free-fall profile (short-dashed magenta) and the sound speed of the hot ambient halo gas c_s (dash-dotted turquoise). Inflow velocities for MN, ART and A_{RP} roughly agree with each other within the 1σ standard deviation, small offsets can be accounted for by the slightly different redshifts.

locities of the inflowing cold streams and not at the average velocity of some net inflow we have to discriminate between the inflowing material belonging to the cold streams and the ambient halo material. We experimented with different cuts and found out that a simple inflow criterion was sufficient. So the velocities are computed by averaging the radial velocity component of all inflowing cells or particles in a given radius bin. Only cells and particles with negative radial velocities are taken into account, i.e. all motion perpendicular to the radial infall direction as well as all cells or particles which are moving outwards are completely neglected. The resulting values are averaged over all available galaxies in the respective mass and redshift bin. Velocities are always quoted dimensionless, namely in units of the virial velocity v_{vir} which has already been defined in equation (5). The resulting profiles are shown in figures 2 (MN), 3 (ART) and 4 (A_{RP}). Free-fall profiles are over-plotted in dotted magenta and the sound speeds of the ambient gas is over-plotted in dash-dotted turquoise. The most striking feature visible is that the velocity is to a very good approximation constant with radius. It is clearly not free-falling. This is the case for all three suites of simulations, for all redshifts or masses as well as for all three constituents: gas, stars or dark matter. The potential energy of the inflowing gas is not converted into kinetic energy, it has to be dissipated by another mechanism, most likely by $\text{Ly}\alpha$ -radiation (Goerdt et al. 2010). In some of the cases however the velocity of the gas follows the sound speed profiles of the hot ambient medium fairly well. Looking at the graphs more carefully the following deviations from constant velocity inflow can be found: MN’s high mass haloes ($M_{\text{vir}} \geq 5 \times 10^{12} M_{\odot}$) have decreasing inflow velocities with decreasing radius. In most of the ART and A_{RP} galaxies on the other hand an increase of the velocity can be seen as the material falls further in. This infall however is far from being consistent with free-fall as the overlain profiles demonstrate. In all other cases the inflow velocity is indeed constant. Additionally there is a dependency of the shape of the inflow velocity profiles with mass and redshift: For low mass haloes ($M_{\text{vir}} \leq 5 \times 10^{12} M_{\odot}$) at high redshift ($z \gtrsim 1.7$) usually there is an increase of velocity with decreasing radius down to $\sim 0.5 r_{\text{vir}}$ from where the velocity is decreasing again. This behaviour originates in the loss of angular momentum due to strong torques in a tilted extended ring, the “strong-torque phase” of the inflow (Danovich et al. 2014, their section 5 and figure 20). For very high mass haloes ($M_{\text{vir}} > 2.5 \times 10^{12} M_{\odot}$) the inflow velocity is slightly increasing with increasing radius over the whole radius range without ever turning down again. In the remaining bins the inflow velocity is constant or only very mildly increasing of with decreasing radius also over the whole radius range also without ever turning down again.

The velocities of the star particles with negative radial velocities stay remarkably constant over the whole radius range for all masses and redshifts. The velocities of the dark matter particles with negative radial velocities increase with increasing radius for high mass galaxies ($> 3 \times 10^{12} M_{\odot}$) and decrease with increasing radius for low mass galaxies ($< 3 \times 10^{12} M_{\odot}$). One would naively expect that at least the dark matter particles inflow velocities would follow free-fall, since those are collision-less and therefore cannot be slowed down by any baryonic processes. However there is no meaningful dark matter accretion within $\sim 2 r_{\text{vir}}$ as already pointed out

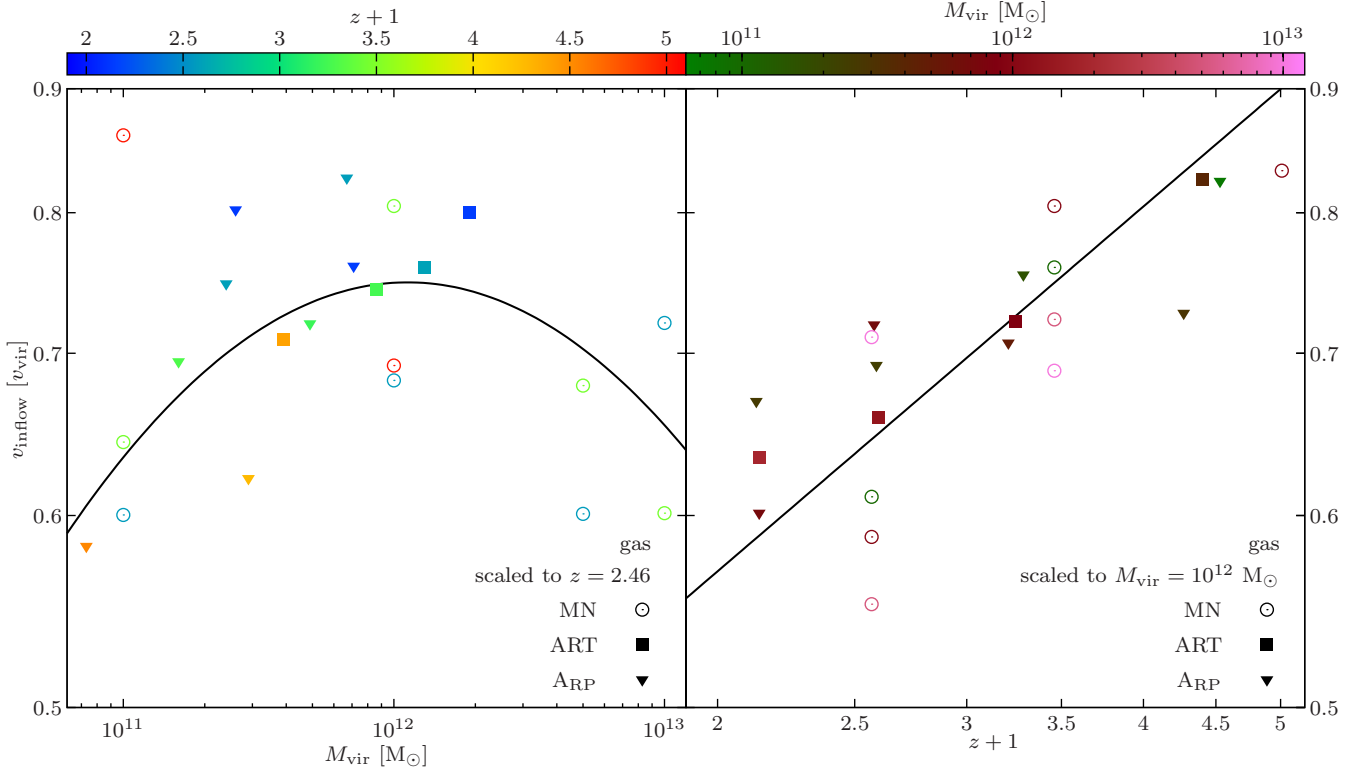


Figure 6. Average inflow velocity v_{inflow} in units of the virial velocity as a function of virial mass M_{vir} (left) or as a function of redshift $z+1$ (right). There is a strong square root power law relationship between the inflow velocity and the redshift (right panel). The inflow velocity also follows a “parabola-like” relation with respect to the host halo mass on the other hand that peaks roughly at $M_{\text{vir}} = 10^{12} M_{\odot}$ (left panel). The data points within each panel were scaled with the help of the scaling relation in the respective other panel to the values indicated. Both scaling relations were found together in an iterative process (see text). The colour bar axes indicate the values the data points used to have before rescaling.

by Cuesta et al. (2008) or Wetzel & Nagai (2014). Therefore the dark matter particles are not inflowing within the radius range analysed, they are just moving back and forth.

The finding of constant velocity inflow is in contrast to earlier works (Faucher-Giguere et al. 2010; Rosdahl & Blaizot 2012). These authors report evidence for free-fall behaviour of the cold streams. A possible explanation for the discrepancies with Faucher-Giguere et al. (2010) might be, that they deployed SPH simulations which used to have inaccuracies modelling dissipative processes (Agertz et al. 2007). Such processes are taking place frequently at the boundary layers of cold streams. Rosdahl & Blaizot (2012) on the other hand used AMR techniques, like us. Their sample of galaxies however was small (only three galaxies in total) and they report that not all of their galaxies showed signs of free-fall behaviour. Constant velocity inflow on the other hand is in agreement with the results from Teklu (2012). She finds constant velocity profiles at around 170 km s^{-1} for three galaxies with $M_{\text{vir}} = 1.5 \times 10^{12} M_{\odot}$ at $z = 2.33$ in her simulations. Strictly non free-falling inflow is also in agreement with the results from Wetzel & Nagai (2014, their figures 4 and 6) who see a decrease in velocity with decreasing radius (roughly a decrease of 65% between $1 r_{\text{vir}}$ and the centre of the host). Unlike us they did not exclude outflowing cells and particles which explains their with radius varying velocities as well as the on average lower values of their speeds.

To guarantee the consistency of the MN, the ART and the ARP simulations it is necessary to compare them directly. In figure 5 galaxies at $z \sim 2.3$ with $M_{\text{vir}} \sim 8 \times 10^{11} M_{\odot}$ are shown for the three suites of simulations. The lines for stars and dark matter are very similar for all three: the velocities are roughly constant over the whole radius range at comparable values. However the gas curves are slightly different: the MN one is by and large constant, whereas the ART as well as the ARP one increase slightly with decreasing radius. The overall increase is roughly 35 % over the whole radius range ($1.7 - 0.2 r_{\text{vir}}$). These increases, as mentioned earlier, are not consistent with free-fall. There is an offset in the values: the MN velocities are $\sim 30\%$ higher over most of the radius range. The offset can be accounted for by the offsets, the host haloes’ masses and redshifts have.

After the consistency of the infall velocities in all three suites of simulations has been established one can now look at possible trends of the infall velocities with mass and redshift. We want to quantify the qualitative statements made earlier. For simplicity a constant infall velocity with radius is assumed. Its actual value is determined by a constant line fit through the velocity curve of the respective mass-redshift bin. The average inflow velocities v_{inflow} of the gas are shown as a function of halo mass M_{vir} and redshift z in figure 6. Plotted are in both panels all available bins of galaxies from MN, ART and ARP as listed in table 1. In the left panel the v_{inflow} values are plotted against the halo mass (M_{vir}) and

in the right panel against redshift ($z + 1$). One can easily identify that the v_{inflow} values in the right panel follow a square root power law with respect to $z + 1$. The best fit square root power law is over-plotted by the solid black line. The v_{inflow} values in the left panel however seem to follow a “parabola-like” function. It is a log-normal distribution function which appears on a log-log plot as a parabola. The function peaks at $M_{\text{vir}} = 10^{12} M_{\odot}$. For the sake of simplicity we will refer to this kind of function as “parabola-like” throughout the paper. The v_{inflow} values of most data points in both panels had to be rescaled in the following way: The v_{inflow} values of the data points within the left panel that were not at $z = 2.46$ were scaled to this value according to the scaling relation presented in the right panel. Likewise the v_{inflow} values of the data points within the right panel whose underlying galaxy bins were not at $M_{\text{vir}} = 10^{12} M_{\odot}$ had to be rescaled to that value according to the scaling relation presented in the left panel. The colour bar axes in both panels indicate the values the galaxy bins used to have before rescaling. Both scaling relations were found in the following iterative process: First a square root power law was fit through the data points in the right panel. This relation was then been used to rescale the data points in the right panel. Subsequently a log-normal distribution function was fit through the (scaled) data points in the left panel. Afterwards the resulting log-normal distribution function was used to rescale the data points in the right panel. These steps have been repeated until convergence was reached (i.e. until the resulting scaling relations did not change anymore). Convoluting the square root power law with the log-normal distribution function leads to the following equation which serves as a model describing the behaviour of the cold stream infall velocity as a function of redshift and host halo mass:

$$\frac{v_{\text{inflow}}(M_{\text{vir}}, z)}{v_{\text{vir}}(M_{\text{vir}}, z)} = \frac{A \sqrt{z+1}}{\sigma (M_{\text{vir}}/M_{\odot})} \times \exp \left\{ -\frac{[\ln(M_{\text{vir}}/M_{\odot}) - \mu]^2}{2 \sigma^2} \right\} \quad (7)$$

Best fit parameter are $A = (2.35 \pm 0.25) \times 10^{16}$, $\mu = 45.4 \pm 4.8$ and $\sigma = 4.20 \pm 0.53$. A visualisation of this 3D functional fit is shown in figure 7, where the values that are actually measured from the simulations are given by the colour within the open symbols as well as by the attached labels. The ART results are represented by squares, the A_{RP} results by triangles and the MN results by circles. Shown as background colour is the fitting function (equation 7) with contour lines at 0.5, 0.6, 0.7, 0.8 and 0.9 v_{vir} .

We are aware of the fact that the choice of a “parabola-like” function instead of another power law as a scaling relation for the data points in the left hand side panel of figure 6 hinges only on the four very high mass ($M \geq 5 \times 10^{12} M_{\odot}$) data points of the MN simulation which is the one having the lowest resolution. We decided to trust these data points anyway since they were at the high mass end of our collection of galaxies were resolution issues play only a minor role. Unfortunately they were no ART or A_{RP} galaxies available in this mass range. On the other hand we decided to neglect the MN data point at $M_{\text{vir}} = 10^{11} M_{\odot}$ and $z = 4.01$ having a very high inflow velocity as an outlier since it has a very low mass, so it might be more prone to resolution effects.

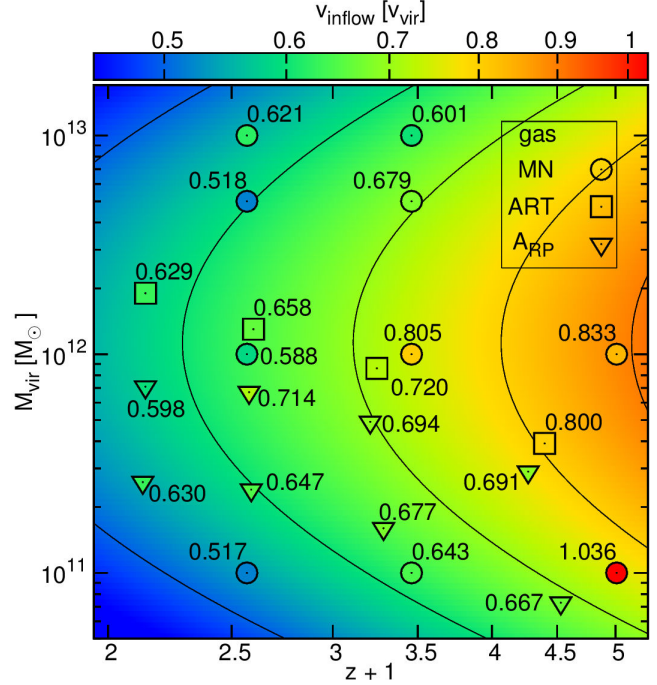


Figure 7. Average inflow velocity of the gas in units of the virial velocity as a function of halo mass and redshift. Shown as background colour is the fitting function (equation 7) with contour lines at 0.5, 0.6, 0.7, 0.8 and 0.9 v_{vir} . The actual values measured from the simulations are given with colour coding within the open symbols as well as by the attached labels. ART is marked by squares, MN by circles and A_{RP} by triangles.

5 CONCLUSIONS

In this paper we looked at the radial inflow velocities of accretion along streams from the cosmic web into massive galaxies at high redshifts using three sets of AMR hydro-cosmological simulations. We calculated free-fall profiles as well as sound speeds of the hot ambient medium via two different methods and we found:

- The velocity profiles for the cold streams in the simulations are very different from free-fall.
- Not even the infall velocities of the dark matter particles follow free-fall, since there is no meaningful dark matter accretion within $\sim 2 r_{\text{vir}}$ of the central halo (Cuesta et al. 2008; Wetzel & Nagai 2014). Therefore the dark matter particles are not inflowing they are rather moving back and forth.
- The sound speed of the ambient medium is a better proxy for the behaviour of the gas inflow velocity, at least at high redshifts. We present a neat scaling relation for the inflow velocity based on this as a first order approximation ($v_{\text{inflow}} = 0.9 v_{\text{vir}}$).
- The velocity profiles for the cold streams are by and large constant with radius or only very slowly increasing with decreasing radius.
- There is a dependence of the shape of the gas infall velocity profiles with mass and redshift: For low mass haloes ($M_{\text{vir}} \leq 5 \times 10^{12} M_{\odot}$) at higher redshift ($z \gtrsim 1.7$) one usually sees an increase of velocity with decreasing radius down to $\sim 0.5 r_{\text{vir}}$ from where the velocity is decreasing again.

This originates in the loss of angular momentum during the “strong-torque phase” (Danovich et al. 2014).

- For very high mass haloes ($M_{\text{vir}} > 2.5 \times 10^{12} M_{\odot}$) the inflow velocity is slightly increasing with increasing radius over the whole radius range. In all other cases the inflow velocity is constant or very mildly increasing of with decreasing radius also over the whole radius range.

- This constant infall velocity has in units of the virial velocity as a function of radius a “parabola-like” dependency on the host halo mass that peaks at $M_{\text{vir}} = 10^{12} M_{\odot}$ and it also follows a square root power law relations with respect to the redshift ($v_{\text{inflow}} \propto \sqrt{z+1} v_{\text{vir}}$).

A potential limitation of our simulations could arise from the artificial pressure floor used in the simulations to ensure that the Jeans mass is always fully resolved. It might affect the temperature and density of the very dense and cold parts of the streams, with implications on the computed inflow velocities. Also the interaction between outflows and inflows is yet to be studied in simulations with strong feedback. Indeed preliminary results of House & Dekel (in preparation) show that there is no strong effect of strong feedback onto inflows. But AMR codes are still the best available tool for recovering the stream properties. With their 17 pc resolution, and with proper cooling below 10^4K , these simulations provide the most reliable description of the cold streams that are available so far.

We conclude that the velocity profile of the gas flowing into a galaxy’s halo in the form of cold streams is, contrary to what might be expected, roughly constant with radius instead of free-falling. The potential energy of the gas which is lost on its way is not converted into kinetic energy but must be dissipated by other mechanisms, such as Ly α radiation (Goerdt et al. 2010).

ACKNOWLEDGEMENTS

Tobias Goerdt is a Lise Meitner fellow. We thank Romain Teyssier for his kindness in sharing simulation data with us. We acknowledge stimulating discussions with Yuval Birnboim and Oliver Czoske. The simulations were performed at the astro cluster at the Hebrew University of Jerusalem, at the National Energy Research Scientific Computing Centre, Lawrence Berkeley National Laboratory and at NASA Advanced Supercomputing at NASA Ames Research Center. Parts of the computational calculations were done at the Vienna Scientific Cluster under project number 70522. The authors would like to thank Jorge Sánchez Almeida and the Instituto de Astrofísica de Canarias for their hospitality, where parts of this work were carried out. This work was supported by FWF project number M 1590-N27.

REFERENCES

Agertz O. et al, 2007, MNRAS, 380, 963
 Agertz O, Teyssier R, Moore B, 2009, MNRAS, 397L, 64
 Agertz O, Teyssier R, Moore B, 2011, MNRAS, 410, 1391
 Agertz O, Kravtsov A. V, Leitner S. N, Gnedin N. Y, 2013, ApJ, 770, 25
 Birnboim Y, Dekel A, 2003, MNRAS, 345, 349
 Birnboim Y, Dekel A, Neistein E, 2007, MNRAS, 380, 339

Bouché N, Murphy M. T, Kacprzak G. G, Péroux C, Contini T, Martin C. L, Dessauges-Zavadsky M, 2013, Science, 341, 50
 Cacciato M, Dekel A, Genel S, 2012, MNRAS, 421, 818
 Ceverino D, Klypin A. A, 2009, ApJ, 695, 292
 Ceverino D, Dekel A, Bournaud F, 2010, MNRAS, 404, 2151
 Ceverino D, Dekel A, Mandelker N, Bournaud F, Burkert A, Genel R, Primack J, 2012, MNRAS, 420, 3490
 Ceverino D, Klypin A, Klimek E. S, Trujillo-Gomez S, Churchill C. W, Primack J, Dekel A, 2014, MNRAS, 442, 1545
 Ceverino D, Dekel A, Tweed D, Primack J, 2015, MNRAS, 447, 3291
 Ceverino-Rodriguez D, 2008, Ph.D. Thesis, New Mexico State University
 Cox T. J, Jonsson P, Somerville R. S, Primack, J. R, Dekel A, 2008, MNRAS, 384, 386
 Cuesta A. J, Prada F, Klypin A, Moles M, 2008, MNRAS, 389, 385
 Dalla Vecchia C, Schaye J, 2008, MNRAS, 387, 1431
 Danovich M, Dekel A, Hahn O, Ceverino D, Primack J, 2014, arXiv:1407.7129
 Dekel A, Birnboim Y, 2006, MNRAS, 368, 2
 Dekel A. et al, 2009a, Nature, 457, 451
 Dekel A, Sari R, Ceverino D, 2009b, ApJ, 703, 785
 Dekel A, Zolotov A, Tweed D, Cacciato M, Ceverino D, Primack J. R, 2013, MNRAS, 435, 999
 Dubois Y, Teyssier R, 2008, A&A, 477, 79
 Fardal M. A, Katz N, Gardner J. P, Hernquist L, Weinberg D. H, Davé R, 2001, ApJ, 562, 605
 Faucher-Giguere C. A, Kereš D, Dijkstra M, Hernquist L, Zaldarriaga M, 2010, ApJ, 725, 633
 Ferland G. J, Korista K. T, Verner D. A, Ferguson J. W, Kingdon J. B, Verner E. M, 1998, PASP, 110, 761
 Genel S, Dekel A, Cacciato M, 2012, MNRAS, 425, 788
 Genel R. et al, 2006, Nature, 442, 786
 Genel R. et al, 2011, ApJ, 733, 101
 Gnedin N. Y, Hollon N, 2012, ApJS, 202, 13
 Goerdt T, Dekel A, Sternberg A, Ceverino D, Teyssier R, Primack J. R, 2010, MNRAS, 407, 613
 Goerdt T, Dekel A, Sternberg A, Gnat O, Ceverino D, 2012, MNRAS, 424, 2292
 Goerdt T, Burkert A, Ceverino D, 2013, arXiv:1307.2102
 Grevesse N, Sauval A. J, 1998, SSRv, 85, 161
 Haardt F, Madau P, 1996, ApJ, 461, 20
 House H, Dekel A, in preparation
 Ibata R. A. et al, Nature, 2013, 493, 62
 Katz N, Hernquist L, Weinberg D. H, 1992, ApJ, 399, 109
 Kennicutt R. C, 1998, ApJ, 498, 541
 Kereš D, Katz N, Weinberg D. H, Davé R, 2005, MNRAS, 363, 2
 Kereš D, Katz N, Fardal M, Davé R, Weinberg D. 2009, MNRAS, 395, 160
 Komatsu E. et al, 2009, ApJS, 180, 330
 Kravtsov A. V, Klypin A. A, Khokhlov A. M, 1997, ApJS, 111, 73
 Kravtsov A. V, 2003, ApJ, 590, 1
 Krumholz M, Burkert A, 2010, ApJ, 724, 895
 Leitherer C. et al, 1999, ApJS, 123, 3
 Mandelker N, Dekel A, Ceverino D, Tweed D, Moody C. E, Primack J, 2014, MNRAS, 443, 3675

- Miller G. E, Scalo J. M, 1979, ApJS, 41, 513
 Ocvirk P, Pichon C, Teyssier R, 2008, MNRAS, 390, 1326
 Robertson B. E, Kravtsov A. V, 2008, ApJ, 680, 1083
 Rosdahl J, Blaizot J, 2012, MNRAS, 423, 344
 Schaye J, Dalla Vecchia C, 2008, MNRAS, 383, 1210
 Springel V, Hernquist L, 2003, MNRAS, 339, 289
 Teklu A, 2012, Bachelor Thesis, LM University Munich
 Teyssier R, 2002, A&A, 385, 337
 Truelove J. K, Klein R. I, McKee C. F, Holliman J. H,
 Howell L. H, Greenough J. A, 1997, ApJ, 489, 179
 Wetzel A. R, Nagai D, 2014, arXiv:1412.0662
 Woosley S. E, Weaver T. A, 1995, ApJS, 101, 181
 Yepes G, Kates R, Khokhlov A, Klypin A, 1997, MNRAS,
 284, 235